

## Comparison between the surface defects caused by Al<sub>2</sub>O<sub>3</sub> and TiN inclusions in interstitial-free steel auto sheets

Rui Wang<sup>1)</sup>, Yan-ping Bao<sup>2)</sup>, Zhi-jie Yan<sup>1)</sup>, Da-zhao Li<sup>1)</sup>, and Yan Kang<sup>1)</sup>

1) School of Materials Science and Engineering, North University of China, Taiyuan 030051, China

2) State Key Laboratory of Advanced Metallurgy, University of Science and Technology Beijing, Beijing 100083, China

(Received: 7 May 2018; revised: 12 June 2018; accepted: 15 June 2018)

**Abstract:** Al<sub>2</sub>O<sub>3</sub> and TiN inclusions in interstitial-free (IF) steel deteriorate the properties of the steel. To decrease the defects of cold-rolled sheet, it is important to clearly distinguish between the degrees of damage caused by these two inclusions on the surface quality of the steel. In this study, a nanoindenter was used to test the mechanical properties of the inclusions, and the distribution and size of the inclusions were obtained by scanning electron microscopy (SEM). It was found that when only mechanical properties are considered, TiN inclusions are more likely to cause defects than Al<sub>2</sub>O<sub>3</sub> inclusions of the same size during the rolling process. However, Al<sub>2</sub>O<sub>3</sub> inclusions are generally more inclined to cause defects in the rolling process than TiN inclusions because of their distribution characteristic in the thickness direction. The precipitation of Al<sub>2</sub>O<sub>3</sub> and TiN was obtained through thermodynamical calculations. The growth laws of inclusions at different cooling rates were calculated by solidification and segregation models. The results show that the precipitation regularity is closely related to the distribution law of the inclusions in IF slabs along the thickness direction.

**Keywords:** interstitial-free steel; inclusions; nanoindenter; inclusion precipitation

### 1. Introduction

Interstitial-free (IF) steel is widely applied in the auto industry because of its high ductility and good deformation [1–2]. These steels are usually stabilized with titanium, so that the interstitial elements (such as N and C) can be scavenged through the formation of high temperature stable precipitates, Ti(C,N), and then removed from the solid solution [3]. It has been well documented that TiN particles play a role in the fracture mechanisms of steels by acting as void or crack nucleation sites [4]. Aluminum is used in steelmaking process because of its high efficiency and economical deoxidation ability as well as its function in grain size refinement and structural strengthening; therefore, Al<sub>2</sub>O<sub>3</sub> inclusions are the main inclusions in IF steel. Numerous researchers have investigated the harmful effect of Al<sub>2</sub>O<sub>3</sub> and TiN inclusions to steel [5–9], but only few have compared the detrimental effects of Al<sub>2</sub>O<sub>3</sub> and TiN inclusions on IF steel auto sheets.

TiN and Al<sub>2</sub>O<sub>3</sub> inclusions are typical in IF steel, and they

are both hard inclusions. However, in reports, defects of cold sheets caused by Al<sub>2</sub>O<sub>3</sub> inclusions are much more than those caused by TiN inclusions, and the reason is unclear. To improve the quality of IF steel cold sheet and realize “zero defect,” it is necessary to study the rules and mechanism of the effect of the inclusions on cold sheets, explicating the degree of damage caused by Al<sub>2</sub>O<sub>3</sub> and TiN inclusions on cold sheet.

In this study, the mechanical property, distribution, and precipitation of Al<sub>2</sub>O<sub>3</sub> and TiN inclusions were systematically investigated by nanoindentation, scanning electron microscopy/energy-dispersive X-ray spectroscopy (SEM/EDS), and thermodynamical calculations. The study focuses on the difference in the mechanical properties between Al<sub>2</sub>O<sub>3</sub> and TiN and the distribution and precipitation rule of inclusions along the thickness direction.

### 2. Experimental

#### 2.1. Production process

The following process was adopted to produce IF steel at

Corresponding author: Rui Wang E-mail: wangrui@nuc.edu.cn

© University of Science and Technology Beijing and Springer-Verlag GmbH Germany, part of Springer Nature 2019

a certain plant: bottom-blown converter → ladle slag modification treatment → 250-t Ruhrstahl-Heraeus (RH) refining → continuous casting (1347 mm × 240 mm). The converter terminal carbon content is required to be controlled at 0.02wt%–0.04wt%. Before the start of RH refining, the ladle slag was modified. About 20 min after the start of the decarburization in RH vacuum degassing, the carbon content reduced to  $15 \times 10^{-6}$ . After decarburization, Al was used as a deoxidizer, and Ti was added to the liquid steel after deoxidization for 3 min. After RH refining, the steel

ladle was left to stand for about 40 min before casting. The composition of the IF steel used in this study is given in Table 1.

## 2.2. Surface defects of inclusions in cold-rolled sheet

Some types of surface defects were obtained from cold-rolled sheet, as shown in Fig. 1, and were cleaned by acetone and machined into 10 mm × 10 mm. The samples were analyzed by SEM and EDS to discover the reason for the defects.

**Table 1.** Composition of the interstitial-free steel

wt%

C	Si	Mn	P	S	Als	Ti	N	T.O	Fe
0.0018	0.0036	0.095	0.0094	0.007	0.04	0.062	0.0022	0.0015	Bal.

Note: Als—soluble aluminium in the steel; T.O—total oxygen in the steel.

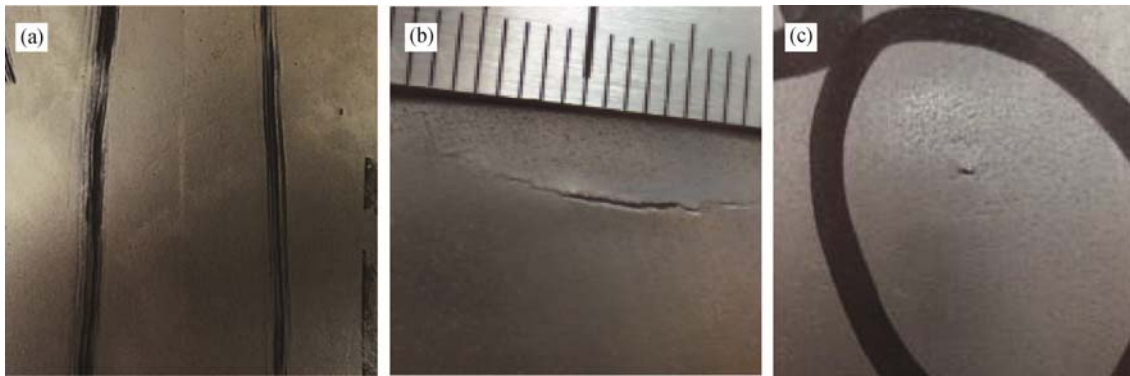


**Fig. 1.** Surface defects of cold-rolled sheet: (a) silver defect; (b) crack; (c) needle-like defect.

## 2.3. Characterization of inclusion by nanoindentation

Rectangular pieces (50 mm × 50 mm × 240 mm), which were taken at 1/4 of the slab (1347 mm × 240 mm) along the width, were machined, and as-cast and as-rolled samples of 10 mm × 10 mm were taken from the pieces and detected by a nanoindenter under the same heat and for each type of inclusion. For an exact analysis, the size of tested inclusions had to exceed 5 μm. Loads were penetrated into the samples at a depth of 120–500 nm, and the hardness was determined as a function of indentation depth. Load–displacement curves were obtained by unloading method, and the hardness ( $H$ ) and elasticity modulus ( $E$ ) were calculated by the Oliver and Pharr (O & P) method [10]. The equations for calculations are shown as follows:

$$H = \frac{P}{A_c} \quad (1)$$

$$E_r = \frac{1}{\beta} \frac{\sqrt{\pi}}{2} \frac{S}{\sqrt{A_c}} \quad (2)$$

$$\frac{1}{E_r} = \frac{1-v^2}{E} + \frac{1-v_i^2}{E_i} \quad (3)$$

where  $A_c$  is the contact area,  $\beta$  is a constant (1.034),  $S$  is the contact stiffness and also the slope of unloading curve,  $E_r$  is the reduced elastic modulus,  $E_i$  is the elasticity modulus of diamond indenter,  $v_i$  is the Poisson ratio of diamond indenter,  $E$  is the elasticity modulus of the tested material, and  $v$  is the Poisson ratio.

## 2.4. Distribution of inclusions along thickness direction

Rectangular pieces (50 mm × 50 mm × 240 mm), taken at 1/4 of the slab (1347 mm × 240 mm) along the width, were machined, and seven metallographic samples (10 mm × 10 mm), labelled from A to G, were successively taken from the inner arc to the center of the rectangular piece, as shown in Fig. 2. These samples were polished with SiC papers and diamond suspensions for the characterization of the inclusions through SEM and EDS. Cylinders (ϕ5 mm × 50 mm), taken at 1/4 of the rectangular piece along the width, were machined for the measurement of the oxygen and nitrogen contents by the infrared absorption method. Other elemental compositions were obtained via the inductively coupled plasma-atomic emission spectrometry method.

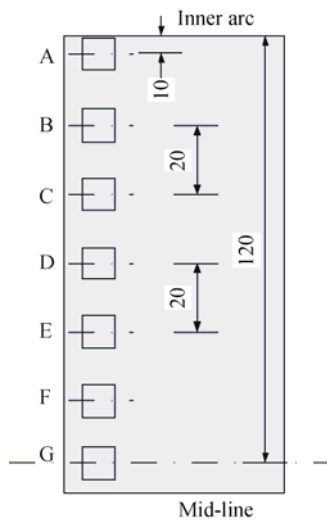


Fig. 2. Schematic diagram of processing of samples (mm).

Each metallurgical sample was observed with 100 fields at 3000 times magnification by SEM. Total area of the field of view was about  $0.88 \text{ mm}^2$  per sample. Inclusion type, quantity, and size were counted and analyzed, according to the observations of each field.

### 3. Results and discussion

#### 3.1. Surface defects of cold-rolled sheets caused by inclusions

Figs. 3(a)–3(c) correspond to the defects in Figs. 1(a)–1(c). Large  $\text{Al}_2\text{O}_3$  inclusions were crushed into small bulks during cold rolling (Fig. 3(a)), which caused a silver defect. The  $\text{Al}_2\text{O}_3$  inclusions were present at the root of cracks (Fig. 3(b)), from where the cracks germinated. The  $\text{Al}_2\text{O}_3$  inclusion led to voids, which emerged near the inclusion during cold rolling (Fig. 3(c)); this is the initiation of needle-like defect.

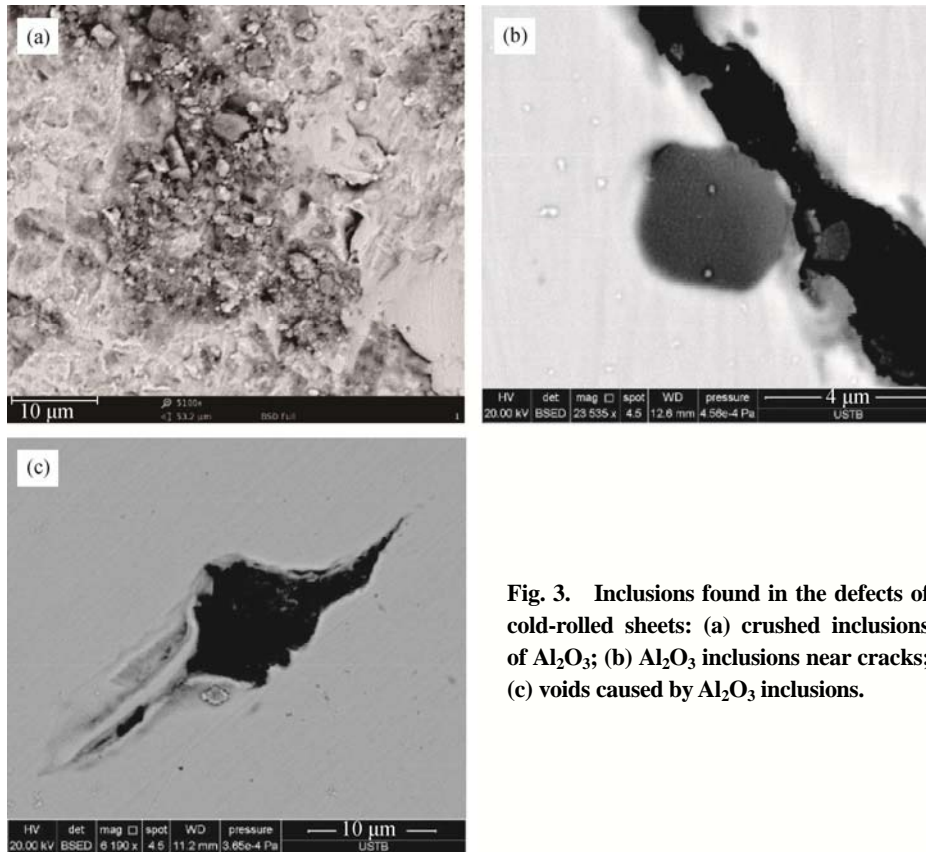


Fig. 3. Inclusions found in the defects of cold-rolled sheets: (a) crushed inclusions of  $\text{Al}_2\text{O}_3$ ; (b)  $\text{Al}_2\text{O}_3$  inclusions near cracks; (c) voids caused by  $\text{Al}_2\text{O}_3$  inclusions.

#### 3.2. Mechanical properties of TiN and $\text{Al}_2\text{O}_3$ inclusions

The results of nanoindentation tests are shown in Table 2. Because of the smaller size of TiN, it was difficult for the indenter to absolutely hit the inclusion; therefore, few data were obtained on TiN inclusions, but the results are similar to those of Ref. [11]. Table 2 shows that in as-cast and rolled states, the average hardnesses of  $\text{Al}_2\text{O}_3$  inclusions were

2.935 and 2.528 GPa, respectively, and the hardnesses of TiN inclusions were 12.200 and 12.603 GPa, respectively. The hardnesses of matrixes in as-cast and rolled states were 1.872 and 1.739 GPa, respectively. This shows that the hardnesses of  $\text{Al}_2\text{O}_3$  and TiN inclusions were much higher than that of the matrix, and the hardness of TiN was about 7 times as high as that of the matrix. These inclusions tend to cause defects in the rolling process.

**Table 2.** Mechanical properties of TiN and Al<sub>2</sub>O<sub>3</sub> inclusions by nanoindentation tests

Sample	Inclusion	Hardness / GPa	Modulus / GPa	Max load / mN	Displacement at max load / nm
As-cast state	Al <sub>2</sub> O <sub>3</sub>	3.029	227.376	8.833	321.032
	Al <sub>2</sub> O <sub>3</sub>	2.759	256.899	6.499	310.042
	Al <sub>2</sub> O <sub>3</sub>	3.019	219.101	6.890	308.076
	Al <sub>2</sub> O <sub>3</sub>	2.998	215.522	6.838	308.081
	Al <sub>2</sub> O <sub>3</sub>	2.966	216.890	6.840	309.581
	TiN	12.200	300.931	28.730	319.563
	Base metal	1.896	202.614	5.473	313.938
	Base metal	1.811	214.612	5.317	315.855
	Base metal	1.828	174.438	5.412	319.466
	Base metal	1.952	220.839	5.849	319.929
Rolled state	Al <sub>2</sub> O <sub>3</sub>	2.437	229.992	5.727	309.269
	Al <sub>2</sub> O <sub>3</sub>	2.591	203.659	6.059	310.604
	Al <sub>2</sub> O <sub>3</sub>	2.590	263.809	6.089	308.660
	Al <sub>2</sub> O <sub>3</sub>	2.494	180.510	5.757	309.513
	TiN	12.603	307.347	76.872	518.126
	Base metal	1.731	194.082	4.650	301.183
	Base metal	1.747	167.379	4.764	301.675

Fig. 4 shows the displacement–load curves of the inclusions and matrix. Fig. 4(a) shows that the residual indentation depth of Al<sub>2</sub>O<sub>3</sub> was deeper than that of TiN, which illustrates that TiN inclusions had better elastic resilience, and Al<sub>2</sub>O<sub>3</sub> inclusions had a greater plastic deformation. Fig. 4(b) illustrates that in both as-cast and rolling states, the matrix had a much greater plastic deformation capacity and less elastic resilience than those of the inclusions. From the above, when only mechanical properties are considered, TiN inclusions are more likely to cause defects than Al<sub>2</sub>O<sub>3</sub> inclusions of the same size in the rolling process.

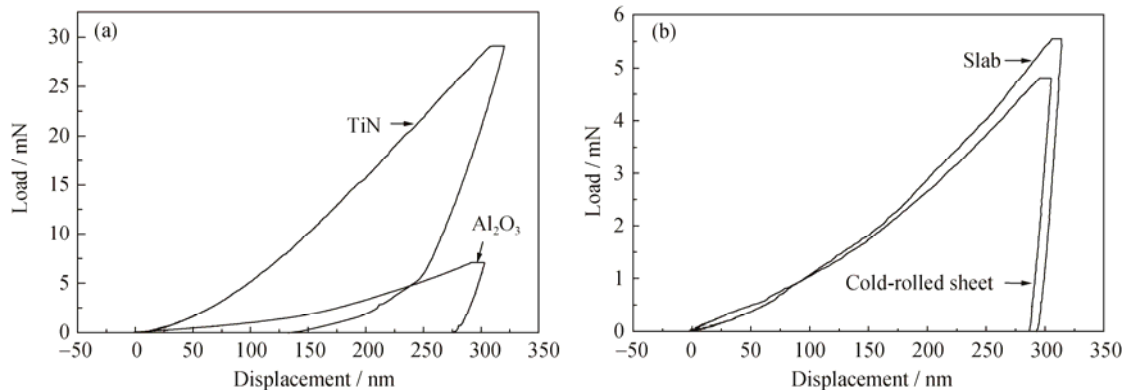
### 3.3. Inclusion quantity and size of IF slabs in the thickness direction

Fig. 5 shows the changes in the number and average size of the inclusions from the inner arc to the center of the slab

along the thickness direction. The number of TiN decreased gradually, while the TiN size increased from the slab surface to the center. The average size of the TiN inclusion was 1.15 μm at the surface, and it increased to 3.80 μm at the center. No rules were observed in the variation of the number and size of Al<sub>2</sub>O<sub>3</sub> inclusion.

The morphologies of Al<sub>2</sub>O<sub>3</sub> inclusions in the slab are shown in Fig. 6. The main inclusions were bulk and circle, and there are several clusters of Al<sub>2</sub>O<sub>3</sub> inclusions (Fig. 6(c)). The size of the inclusions was determined by the longest axis, as shown in Fig. 6.

SEM images of TiN are shown in Fig. 7. According to the TiN images at positions A, D, and G in Fig. 2, more small inclusions were found at the surface of the slab. From the surface to the center of the slab, the number of TiN inclusions reduced and the size gradually increased.

**Fig. 4.** Displacement–load curves of the inclusions (a) and the matrix (b) in interstitial-free steel.

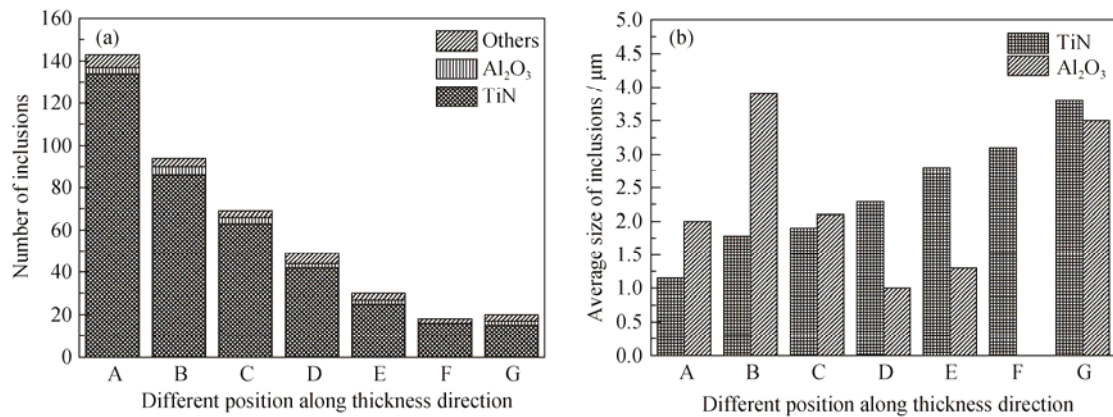


Fig. 5. Characteristic of inclusions at different positions of slab along thickness direction: (a) the number of inclusions; (b) the average size of inclusions.

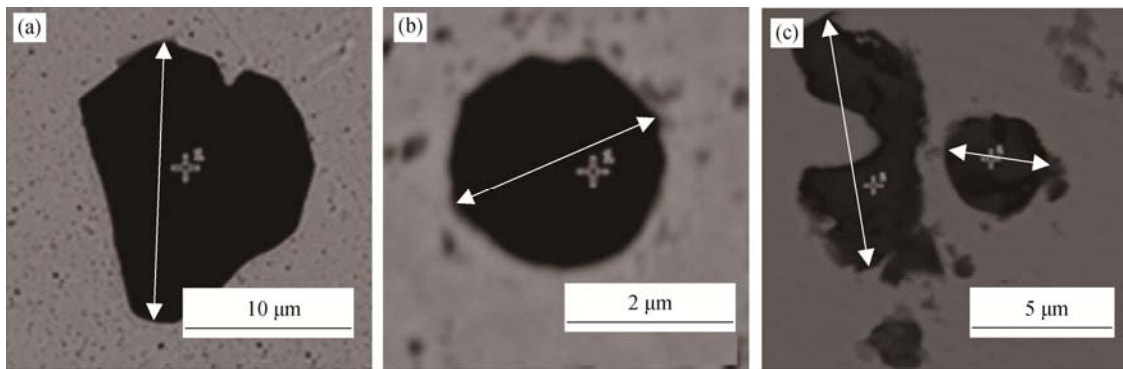


Fig. 6. Morphologies of Al<sub>2</sub>O<sub>3</sub> inclusions in the slab: (a) from position A in Fig. 2; (b) from position C in Fig. 2; (c) from position D in Fig. 2.

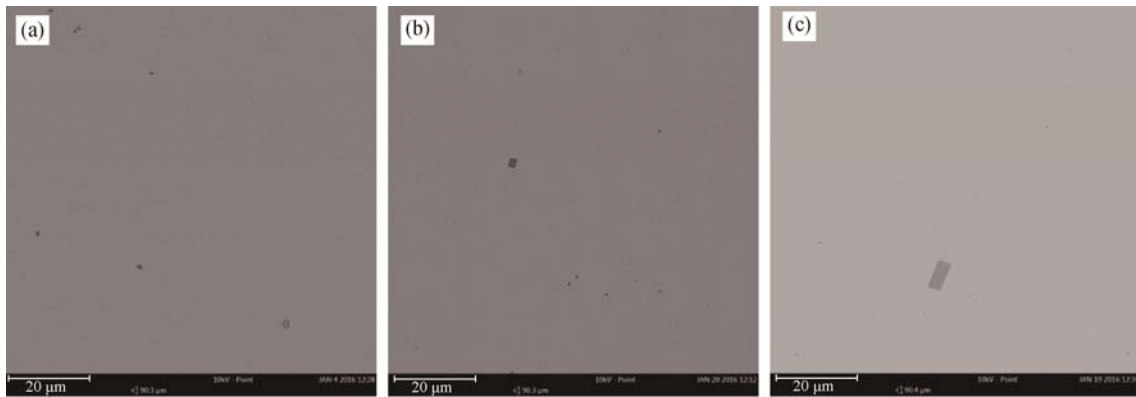


Fig. 7. SEM images of TiN at different positions of the slab along the thickness direction: (a) position A in Fig. 2; (b) position D in Fig. 2; (c) position G in Fig. 2.

Yu *et al.* [12] found that the inclusions had a greater degree of deformation in the rolling process when they were closer to the surface of the billet. Greater deformation means higher stress between the inclusions and matrix, which leads to defects during the rolling process more easily. TiN inclusions became smaller when they were closer to the surface and had an average size of 1.3 μm near the surface of the billet. The Al<sub>2</sub>O<sub>3</sub> inclusions had no distinct distribution near the surface of the billet, and the inclusions were large. In

conclusion, Al<sub>2</sub>O<sub>3</sub> inclusions are more inclined to cause defects in the rolling process than TiN inclusions because of their distribution characteristic along the thickness direction.

### 3.4. Precipitation of inclusions

The reaction between Al and O in the molten steel is described as follows:



FactSage was used to calculate the precipitation temper-

ature of Al<sub>2</sub>O<sub>3</sub> based on the composition of the IF steel shown in Table 1, and it was found that when [Al] and [O] contents were very low in the liquid steel, the Al<sub>2</sub>O<sub>3</sub> inclusions began to precipitate, and the precipitation temperature was above 1950 K (Fig. 8), which is far higher than steelmaking temperature. In the RH process, the oxygen activity in molten steel was generally more than  $300 \times 10^{-6}$  before deoxygenation. When Al was added into steel as a deoxidizer, many Al<sub>2</sub>O<sub>3</sub> inclusions were formed in the liquid steel, which is different from the precipitation of TiN in the solidification process. In summary, the cooling rate had little effect on the precipitation of Al<sub>2</sub>O<sub>3</sub> inclusions, and the size of the inclusions was strongly influenced by the particle collision and polymerization. This is consistent with the results of irregular changes in the number and size of Al<sub>2</sub>O<sub>3</sub> inclusions.

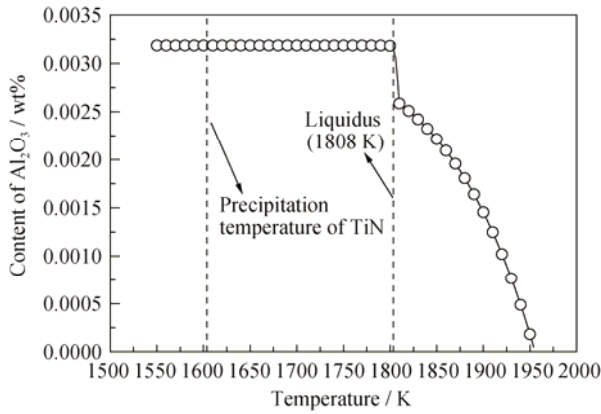


**Fig. 8.** Relationship between Al<sub>2</sub>O<sub>3</sub> and precipitation temperature.

During the solidification process, the uneven cooling in the thickness direction of the slab resulted in different cooling rates in the thickness direction. The growth of the TiN particles formed during solidification at different cooling rates was considered in this study.

In the liquid steel, the Ti content was far greater than the N content; thus, the N content was the limiting factor of the growth of TiN particles. The growth of TiN during solidification can be calculated by the following equation:

$$r \cdot \frac{dr}{dt} = \frac{M_s}{100M_m} \cdot \frac{\rho_m}{\rho_s} D_L (C_L - C_e) \quad (5)$$

where  $r$  is the radius of the TiN particle, m;  $t$  is the solidification time, s;  $M_s$  and  $M_m$  are the mole masses of molten steel ( $56 \text{ g}\cdot\text{mol}^{-1}$ ) and TiN ( $62 \text{ g}\cdot\text{mol}^{-1}$ ), respectively;  $\rho_s$  and

$\rho_m$  are the densities of molten steel ( $7.07 \text{ g}\cdot\text{cm}^{-3}$ ) and TiN ( $5.43 \text{ g}\cdot\text{cm}^{-3}$ ), respectively;  $D_L$  is the diffusion coefficient of N in molten steel,  $\text{m}^2\cdot\text{s}^{-1}$ ;  $C_e$  is the mass fraction of N in equilibrium with TiN; and  $C_L$  is the mass fraction of N during the solidification of molten steel.

During the actual solidification process, the redistribution of solute atoms occurred because of the difference between the solubility of the solid and liquid phases, which resulted in a segregation phenomenon at the solid-liquid interface. Ohnaka equation [13] considers the impact of microsegregation on the concentration of solute elements in liquid steel, as seen in Eq. (6); this equation can study the enrichment behavior of solute atoms in the liquid region during solidification.

$$C_L = C_0 \cdot \left[ 1 - \left( 1 - \frac{\beta k}{1 + \beta} \right) \cdot f_s \right]^{\frac{k-1}{1+\beta}} \quad (6)$$

where  $C_L$  is the mass fraction of solute when the solidification time is  $t$ ;  $C_0$  is the initial mass fraction of solute;  $k$  is the equilibrium partition coefficients of solute atoms in liquid and solid phases;  $f_s$  is the solidification fraction; and  $\beta$  is calculated by

$$\beta = 4D_s\tau/L^2 \quad (7)$$

where  $D_s$  is the diffusion coefficient of solute in the solid phase,  $\text{m}^2/\text{s}$ ;  $\tau$  is the local solidification time, s, which is obtained by Eq. (8); and  $L$  is the secondary dendrite arm spacing,  $\mu\text{m}$ , which is obtained by Eq. (9).

$$\tau = \frac{T_L - T_s}{R_c} \quad (8)$$

where  $T_L$  and  $T_s$  are the temperature of the liquid and solid phase of steel, respectively;  $R_c$  is the cooling rate, K/s.

$$L = 153R_c^{-0.36} \quad (9)$$

According to data of partition coefficients and diffusion coefficient of solute in Table 3,  $\beta$  of Ti and N are obtained, which are all close to 0, and their changes with temperature are little. Taking  $\beta = 0$  into Eq. (6), then the mass fractions of Ti and N in solution are expressed as follows:

$$C(\text{Ti}) = C(\text{Ti})_0 (1 - f_s)^{k_{\text{Ti}} - 1} \quad (10)$$

$$C(\text{N}) = C(\text{N})_0 (1 - f_s)^{k_{\text{N}} - 1} \quad (11)$$

where  $C(\text{Ti})$  and  $C(\text{N})$  are mass fractions of Ti and N in solution;  $C(\text{Ti})_0$  and  $C(\text{N})_0$  are the initial mass fractions of Ti and N in solution, respectively;  $k_{\text{Ti}}$  and  $k_{\text{N}}$  are the partition coefficients of Ti and N.

**Table 3.** Partition coefficients and diffusion coefficient of solute in interstitial-free molten steel

Element	$K$	$D_s / (\text{cm}^2\cdot\text{s}^{-1})$	$D_L / (\text{cm}^2\cdot\text{s}^{-1})$
Ti	0.3 [14]	$68 \times e^{-62400/RT}$ [15]	$3.1 \times 10^{-3} \times e^{-11500/RT}$ [16]
N	0.48 [14]	$7.8 \times 10^{-3} \times e^{-189000/RT}$ [15]	$3.25 \times 10^{-3} \times e^{-11500/RT}$ [14]

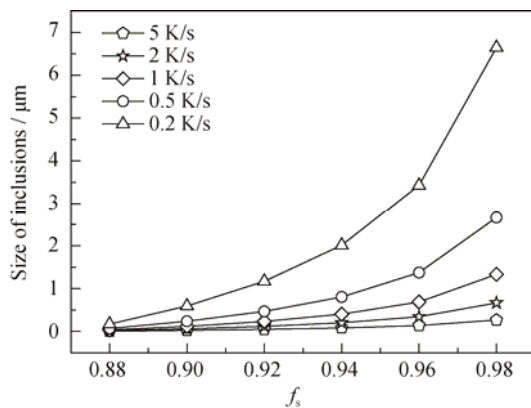


Fig. 9. Effect of the cooling rate on the size of TiN particles.

Through erosion secondary dendrite of slab, Wu *et al.* [17] calculated the cooling rate of the surface and the center of billet as 1.51–4.74 K/s and 0.16–0.32 K/s, respectively. The growth of TiN inclusions in the solidification process at the cooling rates of 5, 2, 1, 0.5, and 0.1 K/s are calculated in this paper, and the results are shown in Fig. 9.

The size of the TiN inclusion was significantly affected by the cooling rate (Fig. 9), indicating that the larger the cooling rate, the smaller the size of the inclusions. The cooling rate in the slab thickness direction gradually increased from the center to the surface; therefore, the size of TiN inclusions gradually decreased, which is consistent with the test results. In addition, because of the large cooling rate and high undercooling, many TiN inclusions precipitated in the surface. However, there was not enough time for the inclusions to grow; thus, many small TiN inclusions were present in the surface.

#### 4. Conclusions

The hardness of TiN inclusions was found to be greater than that of  $Al_2O_3$  inclusions, and the plasticity of TiN inclusions was worse than that of  $Al_2O_3$  inclusions. Therefore, considering only mechanical properties, TiN inclusions are more likely to cause defects in IF steels than  $Al_2O_3$  inclusions of the same size in the rolling process.

The number of TiN decreased gradually, while the TiN size increased from the slab surface to the center, and at the surface, the average size of TiN was 1.15  $\mu m$ , while in the center, the average size was 3.80  $\mu m$ . The changes in the number and size of  $Al_2O_3$  were irregular. Because of their distribution characteristics in the thickness direction,  $Al_2O_3$  inclusions generally are more inclined to cause defects in the rolling process than TiN inclusions.

$Al_2O_3$  inclusions were precipitated at a high temperature in the deoxidation process, so there was no obvious regu-

larity of its distribution in the slab thickness direction. TiN inclusions were precipitated in the solidification process of molten steel; its size had a relationship with the cooling rate; the larger the cooling rate, the smaller the size of the inclusions. Therefore along slab thickness direction, the size of TiN inclusions gradually increased from the surface to the center.

#### Acknowledgement

This work was financially supported by the National Natural Science Foundation of China (No. 51804279).

#### References

- [1] J.L. Guo, Y.P. Bao, and M. Wang, Cleanliness of Ti-bearing Al-killed ultra-low-carbon steel during different heating processes, *Int. J. Miner. Metall. Mater.*, 24(2017), No. 12, p. 1370.
- [2] X.X. Deng, L.P. Li, X.H. Wang, J.Q. Ji, C.X. Ji, and G.S. Zhu, Subsurface macro-inclusions and solidified hook character in aluminum-killed deep-drawing steel slabs, *Int. J. Miner. Metall. Mater.*, 21(2014), No. 6, p. 531.
- [3] R. Kuziak, H. Hartman, M. Budach, and R. Kawalla, Effect of processing parameters on precipitation reactions occurring in a Ti-bearing IF steel, *Mater. Sci. Forum*, 500-501(2005), p. 687.
- [4] O. León-García, R. Petrov, and L.A.I. Kestens, Void initiation at TiN precipitates in IF steels during tensile deformation, *Mater. Sci. Eng. A*, 527(2010), No. 16-17, p. 4202.
- [5] Y. Hu, W.Q. Chen, C.J. Wan, F.J. Wang, and H.B. Han, Effect of deoxidation process on inclusion and fatigue performance of spring steel for automobile suspension, *Metall. Mater. Trans. B*, 49(2018), No. 2, p. 569.
- [6] L.F. Zhang, C.B. Guo, W. Yang, Y. Ren, and H.T. Li, Deformability of oxide inclusions in tire cord steels, *Metall. Mater. Trans. B*, 49(2018), No. 2, p. 803.
- [7] L. Yang, G.G. Cheng, S.J. Li, M. Zhao, G.P. Feng, and T. Li, A coupled model of TiN inclusion growth in GCr15SiMn during solidification in the electroslag remelting process, *Int. J. Miner. Metall. Mater.*, 22(2015), No. 12, p. 1266.
- [8] W.J. Ma, Y.P. Bao, L.H. Zhao, and M. Wang, Control of the precipitation of TiN inclusions in gear steels, *Int. J. Miner. Metall. Mater.*, 21(2014), No. 3, p. 234.
- [9] T. Miyake, M. Morishita, H. Nakata, and M. Kokita, Influence of sulphur content and molten steel flow on entrapment of bubbles to solid/liquid interface, *ISIJ Int.*, 46(2006), No. 12, p. 1817.
- [10] T.Y. Tsui, J. Vlassak, and W.D. Nix, Indentation plastic displacement field: Part II. The case of hard films on soft substrates, *J. Mater. Res.*, 14(1999), No. 6, p. 2204.
- [11] X. Li, Y.P. Bao, and M. Wang, Genetic evolution of inclusions in interstitial-free steel during the cold rolling processes,

*Trans. Indian Inst. Met.*, 71(2018), No. 5, p. 1067.

- [12] H.L. Yu, X.H. Liu, H.Y. Bi, and L.Q. Chen, Deformation behavior of inclusions in stainless steel strips during multi-pass cold rolling, *J. Mater. Process. Technol.*, 209(2009), No. 1, p. 455.
- [13] I. Ohnaka, Mathematical analysis of solute redistribution during solidification with diffusion, *Trans. Iron Steel Inst. Jpn.*, 26(1986), No. 12, p. 1045.
- [14] H.Y. Liu, H.L. Wang, L. Li, J.Q. Zheng, Y.H. Li, and X.Y. Zeng, Investigation of Ti inclusions in wire cord steel, *Iron-making Steelmaking*, 38(2011), No. 1, p. 53.
- [15] J.H. Shang, X.J. Wang, and Y.Z. Chu, Recent development on precipitation behaviour of second-phase particles in Ti-IF steels during hot rolling, *J. Iron Steel Res.*, 12(2000), No. 6, p. 55.
- [16] H. Goto, K.I. Miyazawa, K.I. Yamaguchi, S. Oglibayashi, and K. Tanaka, Effect of cooling rate on oxide precipitation during solidification of low carbon steels, *ISIJ Int.*, 34(1994), No. 5, p. 414.
- [17] H.J. Wu, N. Wei, Y.P. Bao, G.X. Wang, C.P. Xiao, and J.J. Liu, Effect of M-EMS on the solidification structure of a steel billet, *Int. J. Miner. Metall. Mater.*, 18(2011), No. 2, p. 159.